1. Introduction

The nitrogen vacancy (NV) center in diamond is a point defect formed by a substitutional nitrogen atom adjacent to a carbon vacancy within the diamond lattice. This defect exhibits a unique electronic structure, making it one of the most widely studied solid-state quantum systems. NV centers are optically addressable, possess long spin coherence times, and can be initialized, manipulated, and read out at room temperature [1,2].

Owing to these remarkable properties, NV centers have emerged as a versatile platform for a wide range of quantum technologies. Their applications span from components in quantum computing architectures [3] and scalable quantum communication networks [4,5], to platforms for analog quantum simulations [6] and highly sensitive quantum sensors [7–9]. These functionalities rely on the ability to engineer and control NV centers precisely, making their formation and characterization a subject of intense experimental and theoretical research.

A widely used method for creating NV centers in diamond involves the implantation of nitrogen ions into chemical vapor deposited (CVD) diamond followed by annealing at temperatures above 600 °C [10]. During ion implantation, vacancies are generated in the lattice. At room temperature, these vacancies are immobile and remain isolated from the implanted nitrogen atoms.

Substitutional nitrogen atoms introduce local lattice strain due to their slightly larger atomic radius compared to carbon. Upon thermal annealing, the vacancies become mobile and tend to migrate toward and associate with substitutional nitrogen atoms. This pairing relieves local stress and leads to the formation of stable NV centers [11]. The resulting defect complex exhibits exceptional thermal stability. In high-quality diamond, NV centers remain structurally intact up to temperatures of 2000 °C [12].

Nitrogen ion implantation inevitably damages the diamond lattice, leading to the formation of not only NV centers but also a variety of additional defect types. These defects can significantly influence the material's electronic and optical properties, as well as the performance of the NV centers themselves. The subsequent annealing process plays a crucial role in the evolution of the defect landscape. At elevated temperatures, isolated vacancies become mobile and may cluster into larger defect complexes. The nature and concentration of these defects strongly depend on the annealing temperature and can vary substantially, thereby affecting the suitability of the material for quantum applications. A detailed understanding of the types and concentrations of defects present after implantation and annealing is therefore essential for the controlled fabrication of NV-based materials.

In this study, we employ depth-resolved positron annihilation lifetime spectroscopy (PALS), utilizing a pulsed positron beam from the radiation source ELBE, to investigate the defect structure in nitrogen-implanted CVD diamond. Positrons serve as highly sensitive probes for open-volume defects such as vacancies and vacancy clusters [13]. When trapped in such defects, the positron lifetime changes. By analyzing PALS spectra, we gain insights into the presence of different defect species and their concentrations. This allows us to correlate the defect evolution with the annealing conditions and to evaluate their impact on the formation of NV centers.

Two previous publications are directly related to the present work and provide the basis for interpreting our results. In Ref. [14], positron lifetimes for various vacancy-type defects in diamond were calculated using two-component density functional theory. These theoretical lifetimes serve as reference values for the identification and quantitative interpretation of the positron lifetime components observed in the present study. In Ref. [15], diamond samples containing NV centers were illuminated with monochromatic light to induce charge-state conversion of the NV centers, which allowed the detection of NV^+ centers. Building on these earlier studies, the present work focuses on the evolution of different vacancy-type and nitrogen-related defects that form upon nitrogen implantation and subsequent annealing in diamond.

Table 1
Overview of the samples investigated in this study. The listed labels are the short identifiers used consistently in all figures.

№	Sampel	Label in diagrams
1	pristine CVD diamond (as-received)	pristine
2	irradiated with 0.5 MeV N^+ ions	irradiated
3	irradiated and annealed at 600 °C	600 °C
4	irradiated and annealed at 800 °C	800 °C
5	irradiated and annealed at 1000 °C	1000 °C
6	irradiated and annealed at 1200 °C	1200 °C

2. Materials and methods

2.1. Sample preparation

In our study, we used single crystal CVD diamond substrates from ElementSix®with a size of 3×3 mm^2, a thickness of 0.5 mm, and a (100) surface orientation, with both sides polished. According to the manufacturer, the nominal impurity concentrations are below 5 ppb for nitrogen and below 1 ppb for boron.

To generate NV centers, the samples were irradiated with 0.5 MeV N^+ ions at room temperature using the tandem accelerator at the Max Planck Institute for Plasma Physics (IPP) in Garching, Germany. The irradiation was performed under high vacuum conditions ($p < 1\cdot10^{-8}$ mbar) with a fluence of $1\cdot10^{14}$ cm^{-2}. To minimize channeling effects, the samples were mounted with a tilt angle of approximately 3° with respect to the beam axis. The ion beam was scanned over the surface in both x and y directions at 1 kHz to ensure homogeneous implantation. For further experimental details, see [16].

Monte Carlo simulations using the SRIM code [17] indicate a peak nitrogen concentration at approximately 460 nm depth, with the displacement damage maximum located slightly shallower at about 430 nm. The calculations were performed using the "ion distribution and quick calculation of damage" mode with a diamond density of 3.52 g/cm^3 and a displacement energy of 28 eV. It should be noted that SRIM reports only the number of atoms displaced above the energy threshold and does not consider defect clustering or dynamic annealing effects. As the implantation was conducted at room temperature, significant self-annealing is expected, likely leading to an overestimation of the damage, i.e., the number of surviving vacancies, by the SRIM simulation.

Post-implantation annealing was carried out in a vacuum oven using radiant heating. Prior to heating, the quartz glass chamber was repeatedly flushed with argon and evacuated to a pressure of $p < 1\cdot10^{-9}$ mbar. Samples were annealed for 2 h at temperatures of 600 °C, 800 °C, 1000 °C, and 1200 °C, respectively. An overview of all samples investigated in this study is listed in Table 1.

2.2. Depth-resolved positron annihilation lifetime spectroscopy

Positron annihilation lifetime spectra are recorded using the Mono-Energetic Positron Spectroscopy (MePS) setup at the ELBE facility (Electron LINAC for beams with high Brilliance and low Emittance) at the Helmholtz-Zentrum Dresden-Rossendorf (HZDR), Germany [18], which allows for determining the time between positron implantation and annihilation. In this setup, start and stop signals are derived from the pulsing system of the slow positron beam and the 511 keV annihilation γ-quanta, measured by a scintillation detector coupled to a photomultiplier tube. Repeating this sequence for many positrons yields a histogram of annihilation times, from which the characteristic lifetimes and their intensities are extracted. For the implantation energies used here, typical count rates of 5 - 10 kcps result in acquisition times of about 3 - 8 min per spectrum, depending on the chosen positron implantation energy, ranging in this study from 2 to 14 keV.

By varying the positron implantation energy E_{imp}, different depths within the sample can be probed. Increasing E_{imp} shifts the implantation profile to larger depths, but broadens it at the same time [19].

Table 2
Mean implantation depth z_{mean} for each positron implantation energy E_{imp} used in this study. Lower and upper quantiles denote the depths at which the cumulative implantation probability reaches 25 % and 75 %, respectively, around z_{mean}.

E_{imp} (keV)	2	4	6	8	10	12	14
z_{mean} (nm)	23	81	170	286	428	596	788
lower quantile (nm)	−6	−21	−44	−74	−111	−155	−205
upper quantile (nm)	+7	+23	+48	+80	+120	+167	+221

Table 3
Calculated positron lifetimes (in picoseconds) for defect-free bulk diamond and various defect types. These reference values are used to assign experimentally observed lifetimes to specific defect structures. Values are taken from Dickmann et al. [15] and [14].

Perfect bulk	NV^0	NV^-	V_1	V_2	V_3	V_4	V_{10}	V_{20}	V_{30}	V_{40}
103	141	139	145	168	181	198	245	309	338	365

Because the resulting depth distribution is asymmetric, we report the mean implantation depth z_{mean} together with lower and upper quantiles, i.e., the 25th and 75th percentiles, which bracket the central fraction of implanted positrons. The used implantation energy E_{imp}, mean implantation depth z_{mean}, and the corresponding quantiles are summarized in Table 2. All spectra presented in this study contain at least 10^7 counts to ensure sufficient statistical accuracy.

The annihilation radiation is detected using a $CeBr_3$ scintillation detector coupled to a Hamamatsu R13089-100 photomultiplier tube (PMT). The analog output is digitized by an SPDevices ADQ14DC-2X digitizer [20]. The overall time resolution of the system is approximately 220 ps (fwhm), as determined from measurements of a reference sample, i.e., (001) oriented yttria-stabilized zirconia (YSZ), which exhibits a single well-known lifetime.

To extract positron lifetime components, the experimental data are fitted using a model of the form:

$$Z(t) = R(t) * \sum_{i=1}^{n} \frac{I_i}{\tau_i} e^{-t/\tau_i} + \text{Background} \quad (1)$$

Here, $R(t)$ represents the instrument resolution function, modeled as a sum of Gaussian distributions and determined from the YSZ reference measurement. Each term in the sum corresponds to a positron lifetime component with lifetime τ_i and relative intensity I_i. The background is assumed to be constant and close to zero.

The fit is performed using the Levenberg–Marquardt optimization algorithm to minimize the least-squares error between the model and the data. The total intensity is normalized such that $\sum I_i = 1$. The number of components n is chosen to best represent the measured data without overfitting. A comprehensive treatment of the analysis and interpretation of positron lifetime spectra is given in Ref. [13]. For the analysis procedure, we determined the number of lifetime components by gradually increasing the fit complexity and retaining only solutions with stable convergence and reasonable statistics. The resulting components were then checked for physical consistency as a function of implantation energy. In particular, defect signatures observed at neighbouring depths were required to vary smoothly with depth, which excludes isolated extra components without a plausible origin.

To assign a physical interpretation to the lifetime components extracted from the spectra, i.e., to relate measured lifetimes to specific vacancy sizes, we compare them with positron lifetimes calculated for diamond using two-component density-functional theory (TC-DFT). The TC-DFT reference values summarized in Table 3 cover the perfect lattice, small vacancies and larger vacancy clusters, as well as NV centers in the neutral and negative charge states (NV^0, NV^-). In diamond, the positron lifetime increases with the size of the open volume due to the reduced electron density, which provides the basis for mapping measured lifetimes to effective vacancy sizes. Using an empirical relation, a measured lifetime can therefore be mapped to an effective vacancy size n [14]:

$$\tau(n) = A\left(1 - e^{-n/B}\right) + K, \quad (2)$$

where τ is the lifetime component extracted from the spectra and n is the number of missing atoms in the lattice. For diamond, the parameters are $A = 230.3$ ps, $B = 14.3$, and $K = 137.3$ ps [14]. This parameterization is applicable from monovacancies ($n = 1$) up to vacancy clusters of approximately $n = 40$.

Note that when two or more positron lifetime components differ by only a few picoseconds, they cannot be reliably separated in the analysis. In such cases, the fit yields a single “mixed” component whose effective lifetime is mainly governed by the defect state with the highest trapping fraction, i.e., the dominant defect in the material. While the formation of NV centers in nitrogen-doped or nitrogen-implanted diamond is well established, the direct observation of vacancy-cluster nucleation and growth during annealing, and its dependence on the local nitrogen concentration, provides new insight into defect kinetics in diamond. The main contribution of this work is therefore to clarify how vacancy agglomeration competes with NV-center formation and to demonstrate that the presence or absence of nitrogen controls whether vacancies are stabilized as isolated NV-related complexes or incorporated into larger vacancy clusters.

Furthermore, positron lifetimes in defects are determined by the local electron density and can differ for defects located very close to the surface. In our measurements, even the lowest implantation energy (2 keV) corresponds to a mean positron implantation depth of about 23 nm, where bulk-like annihilation conditions prevail. Although back-diffusion could, in principle, lead to trapping at near-surface states, this effect is strongly suppressed in our samples because vacancy-type defects dramatically shorten the positron diffusion length, making a return to the surface highly unlikely.

3. Results

For all samples, depth-resolved PALS was performed as described in Section 2.2. The acquired spectra were analyzed using the multi-component fitting procedure based on Eq. 1.

Fig. 1 displays a representative lifetime spectrum measured at E_{imp} = 10 keV for the pristine diamond sample, together with the corresponding fit. The spectrum can be decomposed into four lifetime components and assigned to distinct annihilation channels. The four independent exponential lifetime spectra with their lifetimes τ_i and their relative intensities I_i are shown, as well as the residuals of the fit. In the example of Fig. 1, the shortest component $\tau_1 \approx 54$ ps represents the reduced bulk lifetime in the presence of strong positron defect trapping. Components between $\sim$ 120 and 500 ps are defect-specific, while components exceeding 500 ps are attributed to positronium formation [13], which can form in larger voids of at least $n \geq 40$ missing atoms or at the crystal surface.

Please note, that the intrinsic bulk lifetime in diamond is $\tau_{bulk} \approx$ 100 ps. At high defect concentrations, the apparent bulk component is reduced, and may even vanish due to saturated trapping [21]. Similar spectra as shown in Fig. 1 were recorded and analyzed for various implantation energies across all samples.

Fig. 2 displays the individual positron lifetime components τ_i extracted from the PALS spectra of all samples as a function of the mean implantation depth z_{mean}. Horizontal bars indicate the central quantile range of the annihilation depth distribution for each energy, as summarized in Table 2. Simulated SRIM data for the nitrogen concentration (green) and the damage (red) are also included. The simulated nitrogen depth profiles are used together with the calculated positron implantation profiles to determine the depth regions in which positrons

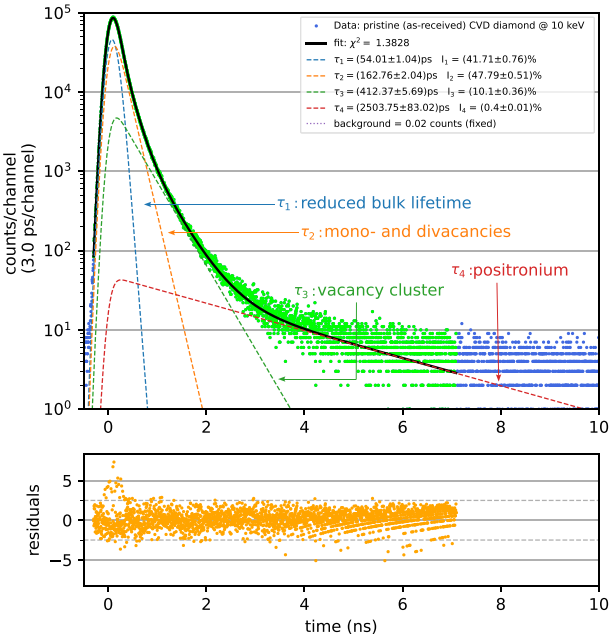


Fig. 1. Positron lifetime spectrum of the pristine diamond sample and its decomposition for E_{imp} = 10 keV: Data points (blue), data used for the fit (green), fit model (black), residuals (orange) and positron lifetime components (dashed lines). (For interpretation of the references to colour in this figure legend, the reader is referred to the web version of this article.)

predominantly annihilate and from which the measured lifetime signal originates. In particular, we distinguish between regions that contain only implantation-induced damage at the pristine nitrogen level, and regions where the nitrogen concentration is significantly increased due to implantation. Although SRIM provides simulations rather than direct measurements, numerous studies have demonstrated that SRIM reproduces the projected range and straggling of nitrogen implantation in diamond with good accuracy, for example the comparison by Healey et al. in Ref. [22]. The same considerations apply to the positron implantation profiles used here, which are likewise derived from established Monte Carlo simulations and carry uncertainties comparable to those of the SRIM calculations. Since the defect distributions vary smoothly with depth and no sharp profile features are required for the analysis, these uncertainties do not affect the conclusions of this work. We therefore conclude that the simulated nitrogen and positron profiles provide a reliable and experimentally supported basis for interpreting the depth-resolved positron annihilation data.

For orientation, the colored background highlights three lifetime regimes corresponding to designated annihilation channels: blue, 0–120 ps (bulk annihilation); gray, 120–210 ps small vacancies (n = 1–5 missing atoms); and orange, 210–500 ps (larger vacancy clusters (n > 5). The corresponding values are derived from density functional theory (DFT) calculations and are taken from [14,15], as summarized in Table 3.

For clarity, only components up to $\tau \leq 500$ ps are shown in Fig. 2. Lifetimes above, if observed, correspond to the annihilation of positronium [13] and are presented separately in Fig. 3. The long-lived lifetime components extracted from the spectra exhibit only very small intensities ($\lesssim$ 7 %). In the nitrogen-implanted samples, these components are limited to a few nanoseconds. Only the pristine diamond shows markedly longer values, reaching up to 17 ns near the surface and decreasing with increasing depth. This behaviour is consistent with positronium formation in surface regions. In the implanted diamonds, however, vacancy-type defects act as highly efficient positron traps, strongly suppressing positronium formation and therefore eliminating such long lifetimes from the spectra.

4. Discussion

As expressed in Eq. (1), each lifetime component τ_i is accompanied by an intensity I_i that represents its fractional annihilation probability. The index assignment ($\tau_1 < \tau_2 < \tau_3 \ldots$) follows purely numerical ordering and does not constitute a physical identification of specific defect types. To enable a physically meaningful comparison, we therefore regroup the intensities according to the lifetime regimes based on the calculated values in Table 3 and defined in Fig. 2. Consequently, Fig. 4 shows the intensities associated with bulk annihilation, small vacancies ($n \leq 5$ missing atoms), and larger vacancy clusters ($n \geq 10$ missing atoms) as a function of the mean implantation depth.

Fig. 5 shows, based on Eq. (2), the effective vacancy sizes n inferred from the respective PALS components at mean implantation depths of approximately 80, 170, and 430 nm.

To estimate the concentrations of the respective vacancy types, we apply the two-defect trapping model [13], which requires the absence of saturated trapping, i.e., a (reduced) bulk lifetime component must be found in the PALS spectrum. Under these conditions, the shortest lifetime τ_1 represents the (reduced) bulk lifetime, while τ_2 and τ_3 are the characteristic lifetimes of two different defect types. The corresponding defect trapping rates $\kappa_i = \mu_i C_i$ then follow as

$$\kappa_1 = \mu_1 C_1 = I_2 \left(\frac{1}{\tau_1} - \frac{1}{\tau_2} \right) , \tag{3}$$

$$\kappa_2 = \mu_2 C_2 = I_3 \left(\frac{1}{\tau_1} - \frac{1}{\tau_3} \right) , \tag{4}$$

where μ_i are the defect-specific trapping coefficients, C_i the defect concentrations, and I_2 and I_3 the intensities of the defect-related components with lifetimes τ_2 and τ_3, respectively.

In many cases the defect-specific trapping coefficient μ_i is unknown. If the monovacancy trapping coefficient μ_0 is known, μ_i can be estimated via [13]:

$$\mu_i = m_i \, \mu_0, \tag{5}$$

where m_i is a size-dependent factor. For small vacancies ($n \leq 5$), it increases linearly with the size ($m_i = n$). For larger defects the growth of m_i gradually saturates because trapping becomes limited due to the finite positron mobility [13].

To calculate the concentrations of defects we use the monovacancy trapping coefficient $\mu_0 = 10^{15}\,\mathrm{s}^{-1}$ reported for diamond by Saarinen *et al.* [23]. For spectra containing a positronium component ($\tau \geq 500$ ps), this component was excluded from the calculations due to its low intensity ($\leq 7\%$). The remaining intensities were then renormalized, so that $I_i = 1$. This procedure affects only the intensities. The fitted lifetimes of the retained components remain unchanged.

Combining Eq. (3) with Eq. (5) allows us to determine borders for the concentrations C_i. The lower bound corresponds to monovacancies with $m_i = n = 1$, whereas the upper bound for small defects is evaluated with $m_i = n = 5$. For larger vacancy clusters the increase of m_i saturates, therefore, only an upper bound can be provided. Based on the measured lifetimes and DFT values indicating that the large clusters comprise at least $n \geq 10$ missing atoms, we suppose $m_i = 10$ as a conservative choice for this upper bound. The resulting concentration estimates are summarized in Fig. 6 for all spectra where the two-defect trapping model is applicable. Please note that only upper and lower limits for the defect concentrations can be given, and that these limits depend on the vacancy size. Our measurements indicate the presence of a distribution of small vacancy-type defects, each containing at most about five missing atoms. Because several different defect types are likely present simultaneously in our samples, we report concentration ranges rather than unique values for individual vacancy species.

For a mean implantation depth of 430 nm, where the nitrogen content and damage reach their maxima, we present the mean concentrations of small vacancies ($n \leq 5$) and large vacancy clusters ($n \geq 10$) in Fig. 7.

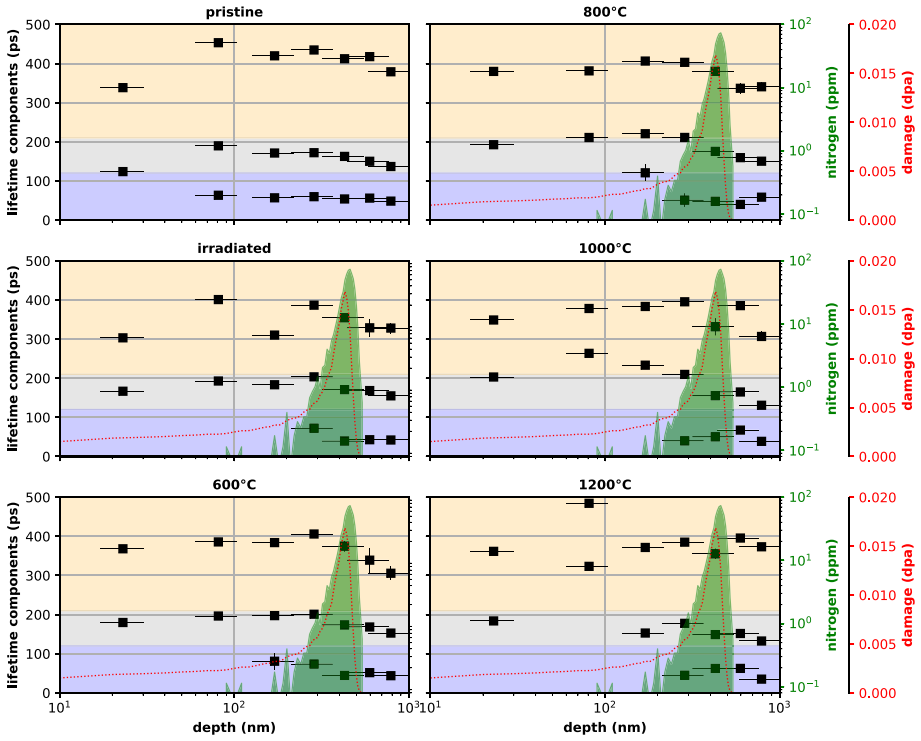


Fig. 2. Positron lifetime components extracted from the measured spectra as a function of implantation depth for the pristine (as-received) CVD diamond, after irradiation (not-annealed) and after annealing at temperatures from 600 - 1200 °C. Shaded background regions indicate characteristic lifetime ranges associated with different vacancy sizes: the blue region (0 – 120 ps) corresponds to annihilation in defect-free bulk, the gray region (120 – 210 ps) to vacancy clusters containing up to 5 missing atoms, and the orange region (210 – 500 ps) to larger vacancy agglomerates. The green area indicates the nitrogen concentration, the red curve the damage as calculated with SRIM. Horizontal bars represent the 25 - 75 % implantation quantiles for positrons, as given in Table 2. Vertical bars, if bigger than the markers, represent the errors derived from the fit. (For interpretation of the references to colour in this figure legend, the reader is referred to the web version of this article.)

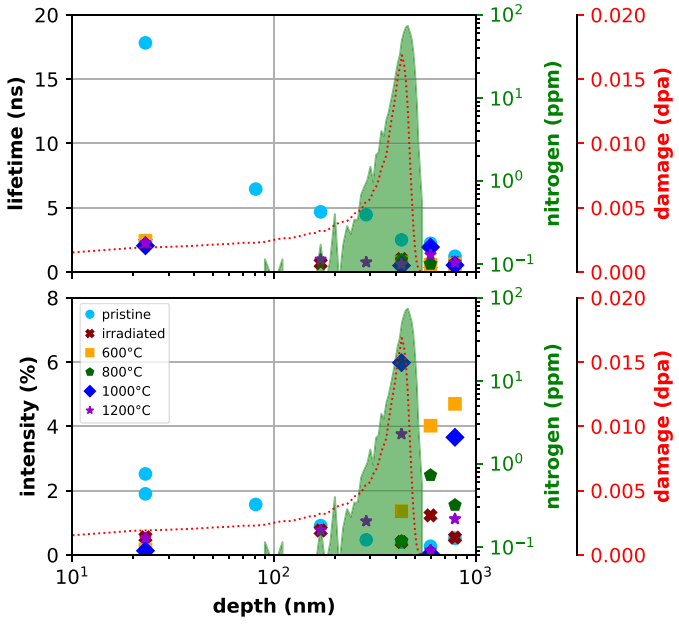


Fig. 3. Positronium-related lifetime components ($\tau \geq 500$ ps) extracted from fits to PALS spectra as a function of the mean implantation depth, together with their corresponding intensities.

4.1. Pristine CVD diamond

Since the pristine CVD diamond serves as the reference, we want to discuss the results obtained with this sample first. As shown in Fig. 2, the lifetime distribution becomes relatively homogeneous for depths $z \geq 80$ nm. The spectra consistently exhibit (i) bulk components with reduced lifetimes, (ii) components characteristic of small vacancy defects ($n \leq 5$ missing atoms), and (iii) components attributable to larger vacancy clusters ($n \geq 40$). In the probed depth range, the mean concentration of small vacancies is about 2.7 ppm, while that of vacancy clusters remains below 1.5 ppm. The lifetime of $\tau_2 = 189$ ps indicates a characteristic vacancy size of ~ 4 missing atoms at $z \approx 80$ nm, as shown in Fig. 5. At greater depths the spectra are dominated by divacancies. This trend is consistent with the thermodynamic driving force for vacancy aggregation, where paired vacancies are energetically favored over isolated monovacancies [24].

The pristine diamond is the only sample in our study, where we found in all measured spectra a long lifetime component $\tau > 500$ ps, which we attribute to positronium formation [13]. Two mechanisms are plausible: (i) back-diffusion of thermalized positrons toward the surface followed by positronium formation, facilitated by the negative positron work function reported for diamond surfaces [25], and (ii) positronium formation within sufficiently large vacancy clusters, which yields distinct long lifetime signatures in the PALS spectra.

We assume that both mechanisms are valid. At shallow implantation depths, back-diffusion enhances the detection of surface positronium. At greater depths, diffusion to the surface becomes unlikely and, consequently, positronium formation in large vacancy clusters dominates the observed signals of long lifetime components.

4.2. Generation of defects during nitrogen implantation

For the irradiated, non-annealed diamond sample, the PALS analysis shows that lifetime components associated with small vacancies carry the largest intensities, i.e., most positrons annihilate after being trapped inside these defects (see Fig. 4). The irradiation-induced defects are

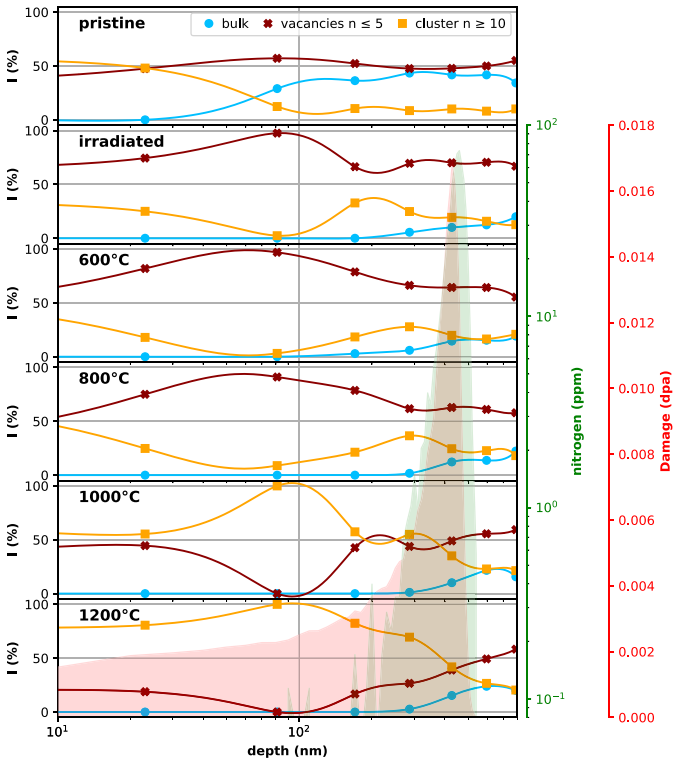


Fig. 4. Lifetime component intensities as a function of implantation depth: (blue) bulk lifetime intensities $\tau \leq 120$ ps, (red) intensities associated with small vacancies ($120 < \tau \leq 210$ ps), and (orange) intensities corresponding to positron annihilation inside vacancy clusters ($210 < \tau \leq 500$ ps). Lines are guides to the eye. (For interpretation of the references to colour in this figure legend, the reader is referred to the web version of this article.)

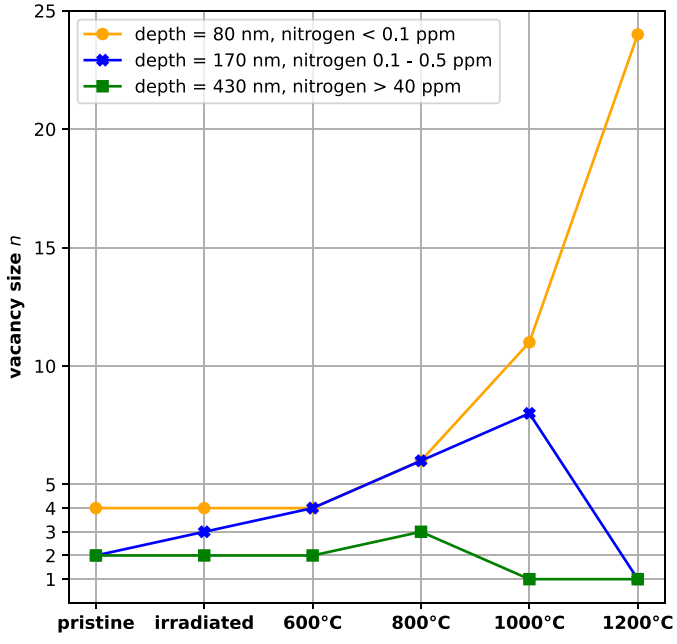


Fig. 5. Effective vacancy sizes n for all samples at three mean implantation depths, inferred from the PALS spectra using the lifetime–to–size mapping in Eq. (2). Lines are added to guide the eye.

predominantly small vacancies ($n \leq 4$) whose concentrations increase relative to the pristine diamond.

In the nitrogen-poor region ($z \leq 170$ nm), the defect density is sufficiently high to cause saturated positron trapping, where no bulk lifetime component is observed. At greater depths, where the nitrogen content exceeds 1 ppm, a reduced bulk component can be found despite higher damage, which enables quantitative concentration estimates. This behavior can be explained by the higher concentration of implanted nitrogen at this depth (compared to shallower regions). The induced damage is occupied by nitrogen atoms at substitutional lattice sites, which limits the resulting damage during implantation. At a depth of ~ 430 nm, the mean concentration of small vacancies rises to ~ 6.3 ppm, compared with ~ 2.7 ppm in the pristine sample. Furthermore, nitrogen irradiation promotes the formation of larger vacancy clusters in this region, with their concentration increasing from approximately 0.1 ppm to 0.3 ppm.

4.3. Defect behavior during annealing

For the diamond sample annealed at 600°C after nitrogen implantation, the PALS analysis indicates that, in nitrogen-rich regions, the defect landscape differs only marginally from the as-implanted sample. The dominant defect type remains the divacancy, with similar concentrations of ~ 5 ppm, alongside large vacancy clusters below ~ 0.3 ppm.

In contrast, within the region, where the nitrogen concentration stays below 1 ppm (170–290 nm), annealing reduces the concentrations of both small vacancies and large clusters to values comparable to the pristine sample. A slightly increased lifetime of the cluster-related component compared with the as-implanted state suggests modest cluster growth, consistent with mobile small vacancies attaching to pre-existing clusters at 600°C.

In the near-surface region ($z < 170$ nm), the defect density remains sufficiently high to cause saturated positron trapping (no bulk component), which prevents a reliable concentration analysis. The predominant defects there are still small vacancies with $n \leq 5$.

With increasing annealing temperature T, a larger fraction of small vacancies becomes mobile and either agglomerates into larger clusters or attaches to pre-existing ones. In the shallow region ($z \leq 170$ nm) saturated positron trapping persists, therefore, absolute concentration estimates are not possible. Nevertheless, the evolution of the fitted intensities indicates progressive cluster growth. As shown in Fig. 4, the cluster-associated intensity at $z \leq 170$ nm reaches its maximum after annealing at $T \geq 1000$°C.

At greater depths, where the nitrogen content is higher, agglomeration of new vacancy clusters or attachment to existing clusters is reduced compared to shallower depths. Although annealing still promotes the formation and growth of vacancy clusters, a bulk lifetime component remains detectable at all temperatures, i.e., total positron trapping is not observed. With increasing T, the concentration of vacancy clusters increases from ~ 0.1 ppm (pristine sample) to ~ 0.3 ppm (irradiated and annealed samples at 600°C and 800°C) to ~ 1 ppm (annealed samples at 1000°C and 1200°C), while that of small vacancies decreases, as shown in Fig. 7. For $T \leq 600$°C the spectra are dominated by divacancies, near 800°C these defects coarsen toward tri-vacancies. At higher temperatures, mobile vacancies are efficiently captured by substitutional nitrogen to form NV centers, which depletes the residual population of isolated small vacancies and limits further coarsening. Vacancies that do not form NV centers tend to be incorporated into existing clusters. Therefore, the apparent decrease in vacancy size at 1200 °C and 170 nm, and at 1000 °C and 1200 °C for 430 nm, shown in Fig. 5, should not be interpreted as a literal shrinking of individual clusters. Rather, it reflects a redistribution of vacancies at high temperature. Mobile vacancies are either captured by nitrogen to form NV centers or other small vacancy-impurity complexes. As a result, positrons are increasingly trapped at

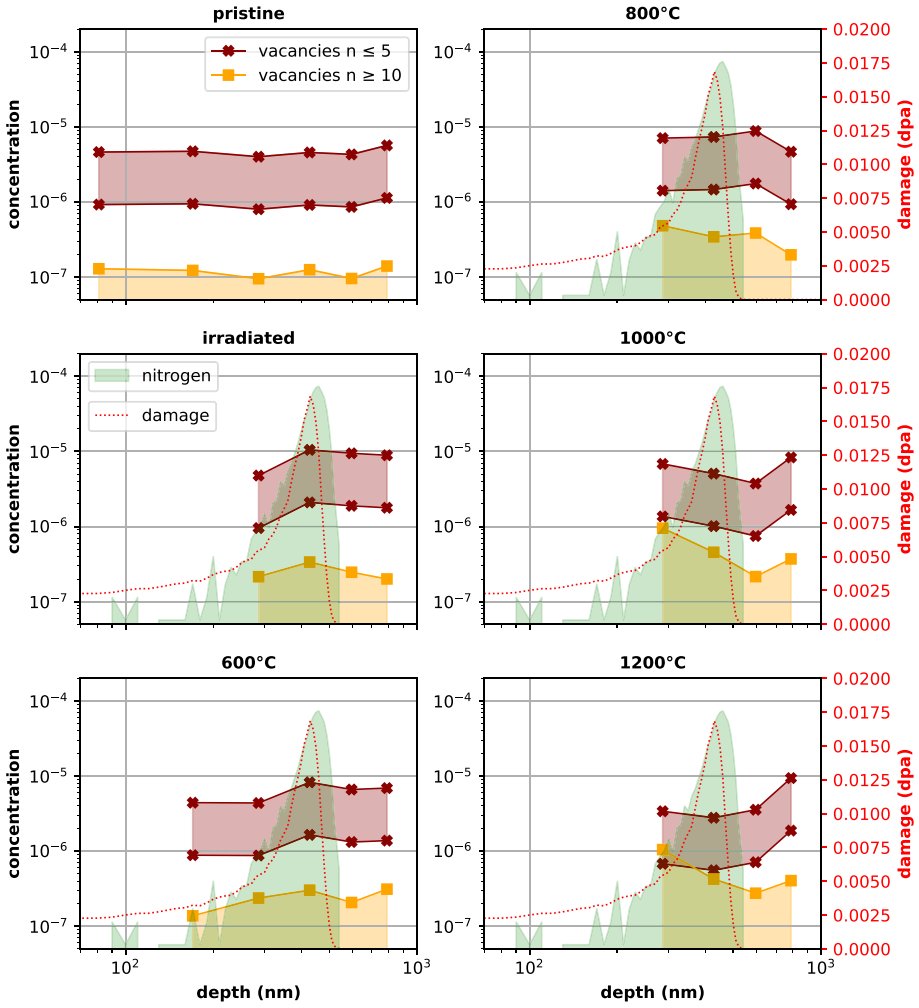


Fig. 6. Defect concentrations as a function of the mean implantation depth in regions without saturated positron trapping. Shown are upper bounds for vacancy clusters ($n \geq 10$) and lower/upper bounds for small vacancies ($n \leq 5$), obtained from the two-defect trapping model. Lines are added to gide the eye.

smaller open-volume defects with shorter lifetimes, so that the effective vacancy size extracted from the lifetime analysis decreases. We emphasize that these changes lie within the uncertainties of the lifetime-size conversion and should be understood as trends in the relative defect populations rather than precise numbers of missing atoms.

A further aspect is the ratio between the concentration of NV centers and the amount of implanted nitrogen. In nitrogen-rich regions and at high annealing temperatures ($T \geq 1000$°C), the defect signatures detected by PALS are consistent with NV-related trapping. Nevertheless, the NV-related concentration is typically about one order of magnitude lower than the local nitrogen concentration. Several mechanisms can account for this discrepancy.

First, positively charged NV centers (NV^+) do not trap positrons, in contrast to NV^0 and NV^-. Photoinduced charge conversion from NV^+ to NV^0 has been reported for photon energies around 1.23 eV [15]. Since our measurements were performed under ambient light, a steady-state population dominated by NV^0/NV^- is expected, making large fractions of invisible NV^+ unlikely.

Second, nitrogen aggregation reduces the number of NV centers per nitrogen atom. Multiple substitutional nitrogen atoms can bind to a single vacancy to form N_2V or N_3V centers [26,27]. N_1V typically forms upon annealing at $\sim$ 800–1100°C [28], may transform into N_2V during prolonged annealing near 1100–1200°C, and further aggregation can yield N_3V at higher temperatures [27]. Such pathways naturally reduce the NV yield relative to the total nitrogen content.

Third, nitrogen incorporates and traps into large vacancy clusters. This can, in principle, reduce the positron lifetime, although this effect becomes weak for large clusters because the positron wave function is dominated by the extended open volume rather than the chemical environment at the boundary. At the same time, vacancy aggregation at high annealing temperatures increases the effective cluster size and thus leads to longer lifetimes. Our measurements show no systematic decrease in the cluster-related lifetime with temperature. This implies that any nitrogen decoration of the dominant large clusters remains below the detection limit.

Fourth, at high temperatures monovacancies can be captured by pre-existing clusters before they meet substitutional nitrogen. In this scenario substitutional nitrogen remains as N_s while the vacancy population is depleted by cluster growth, again lowering the NV yield.

We therefore argue that the lower NV yield relative to the number of implanted nitrogen atoms results from a combination of nitrogen aggregation into N_2V and N_3V (in addition to N_1V) and the kinetic capture of monovacancies by vacancy clusters before N_1V can form.

5. Conclusion

Single-crystal CVD diamonds were implanted with 0.5 MeV nitrogen ions at a fluence of 1×10^{14} cm^{-2} and subsequently annealed between 600°C and 1200°C. The defect evolution was investigated by depth-resolved positron annihilation lifetime spectroscopy.

Declaration of competing interest

The authors declare the following financial interests/personal relationships which may be considered as potential competing interests:

Marcel Dickmann reports that financial support was provided by the German Federal Ministry of Education and Research. If there are other authors, they declare that they have no known competing financial interests or personal relationships that could have appeared to influence the work reported in this paper.

Acknowledgments

The authors thank Dr. Gottfried Kögel for the discussions and the support with data analysis. PALS measurements were carried out at ELBE at the Helmholtz-Zentrum Dresden-Rossendorf e.V., a member of the Helmholtz Association. We would like to thank the facility staff for their assistance. Funding from BMBF project 05K22WN1 “PosiScan” is gratefully acknowledged.

Data availability

Data will be made available on request.

References

[1] P. Neumann, N. Mizuochi, F. Rempp, P. Hemmer, H. Watanabe, S. Yamasaki, V. Jacques, T. Gaebel, F. Jelezko, J. Wrachtrup, Multipartite entanglement among single spins in diamond, Science 320 (5881) (2008) 1326–1329, https://doi.org/10.1126/science.1157233

[2] M.V.G. Dutt, L. Childress, L. Jiang, E. Togan, J. Maze, F. Jelezko, A.S. Zibrov, P.R. Hemmer, M.D. Lukin, Quantum register based on individual electronic and nuclear spin qubits in diamond, Science 316 (5829) (2007) 1312–1316, https://doi.org/10.1126/science.1139831

[3] I. Aharonovich, A.D. Greentree, S. Prawer, Diamond photonics, Nat. Photonics 5 (7) (2011) 397–405, https://doi.org/10.1038/nphoton.2011.54

[4] X.-D. Chen, E.-H. Wang, L.-K. Shan, S.-C. Zhang, C. Feng, Y. Zheng, Y. Dong, G.-C. Guo, F.-W. Sun, Quantum enhanced radio detection and ranging with solid spins, Nat. Commun. 14 (1) (2023) 1288, https://doi.org/10.1038/s41467-023-36929-8

[5] H.J. Kimble, The quantum internet, Nature 453 (7198) (2008) 1023–1030, https://doi.org/10.1038/nature07127

[6] G.L. van de Stolpe, D.P. Kwiatkowski, C.E. Bradley, J. Randall, M.H. Abobeih, S.A. Breitweiser, L.C. Bassett, M. Markham, D.J. Twitchen, T.H. Taminiau, Mapping a 50-spin-qubit network through correlated sensing, Nat. Commun. 15 (1) (2024) 2006, https://doi.org/10.1038/s41467-024-46075-4

[7] D.M. Irber, F. Poggiali, F. Kong, M. Kieschnick, T. Lühmann, D. Kwiatkowski, J. Meijer, J. Du, F. Shi, F. Reinhard, Robust all-optical single-shot readout of nitrogen-vacancy centers in diamond, Nat. Commun. 12 (1) (2021) 532, https://doi.org/10.1038/s41467-020-20755-3

[8] G. Balasubramanian, I.Y. Chan, R. Kolesov, M. Al-Hmoud, J. Tisler, C. Shin, C. Kim, A. Wojcik, P.R. Hemmer, A. Krueger, T. Hanke, A. Leitenstorfer, R. Bratschitsch, F. Jelezko, J. Wrachtrup, Nanoscale imaging magnetometry with diamond spins under ambient conditions, Nature 455 (7213) (2008) 648–651, https://doi.org/10.1038/nature07278

[9] C.L. Degen, F. Reinhard, P. Cappellaro, Quantum sensing, Rev. Mod. Phys. 89 (3) (2017), https://doi.org/10.1103/revmodphys.89.035002

[10] J.R. Rabeau, P. Reichart, G. Tamanyan, D.N. Jamieson, S. Prawer, F. Jelezko, T. Gaebel, I. Popa, M. Domhan, J. Wrachtrup, Implantation of labelled single nitrogen vacancy centers in diamond using N15, Appl. Phys. Lett. 88 (2) (2006).

[11] A.R. Lang, M. Moore, A.P.W. Makepeace, W. Wierzchowski, C.M. Welbourn, On the dilatation of synthetic type ib diamond by substitutional nitrogen impurity, Philos. Trans. R. Soc. Lond. Ser. A Phys. Eng. Sci. 337 (1648) (1991) 497–520.

[12] M.N.R. Ashfold, J.P. Goss, B.L. Green, P.W. May, M.E. Newton, C.V. Peaker, Nitrogen in diamond, Chem. Rev. 120 (12) (2020) 5745–5794.

[13] R. Krause-Rehberg, H.S. Leipner, Positron annihilation in semiconductors: Defect studies; with 20 tables, corr. 2. print Edition, vol. 127 Springer series in solid-state sciences, Springer, Berlin, 2003.

[14] M. Dickmann, R. Helm, W. Egger, J. Mitteneder, J.A. Duffek, P. Jarmatz, G. Dollinger, Ab initio calculations of positron lifetimes in diamond: the bulk, vacancies and grain boundary, Solid State Phenom. 374 (2025) 145–153.

[15] M. Dickmann, L. Mathes, R. Helm, V.V. Burwitz, W. Egger, J. Mitteneder, C. Hugenschmidt, P. Sperr, M. Butterling, M.O. Liedke, et al., Identification and reversible optical switching of NV+ centers in diamond, Adv. Funct. Mater. 35 (2025) 2500817.

[16] T. Schwarz-Selinger, Deuterium retention in MeV self-implanted tungsten: influence of damaging dose rate, Nucl. Mater. Energy 12 (2017) 683–688, https://doi.org/10.1016/j.nme.2017.02.003

[17] R.E. Stoller, M.B. Toloczko, G.S. Was, A.G. Certain, S. Dwaraknath, F.A. Garner, On the use of SRIM for computing radiation damage exposure, Nucl. Instrum. Methods Phys. Res. Sect. B Beam Interact. Mater. Atoms 310 (2013) 75–80, https://doi.org/10.1016/j.nimb.2013.05.008

[18] A. Wagner, M. Butterling, M.O. Liedke, K. Potzger, R. Krause-Rehberg, Positron annihilation lifetime and doppler broadening spectroscopy at the ELBE facility, AIP Conf. Proc. 1970 (1) (2018) 040003, https://doi.org/10.1063/1.5040215

[19] A.F. Makhov, Electron penetration in solids. II. Electron distributions in depth, 2 of Fizika Tverdogo Tela, 1960.

[20] E. Hirschmann, M. Butterling, U. Hernandez Acosta, M.O. Liedke, A.G. Attallah, P. Petring, M. Görler, R. Krause-Rehberg, A. Wagner, A new system for real-time data acquisition and pulse parameterization for digital positron annihilation lifetime spectrometers with high repetition rates, J. Instrum. 16 (8) (2021) P08001, https://doi.org/10.1088/1748-0221/16/08/P08001

[21] P. Hautojärvi, C. Corbel, Positron spectroscopy of defects in metals and semiconductors, in: Positron spectroscopy of solids, IOS Press, 1995, pp. 491–532.

[22] A.J. Healey, A. Stacey, B.C. Johnson, D. Broadway, T. Teraji, D. Simpson, J.-P. Tetienne, L.C.L. Hollenberg, Comparison of different methods of nitrogen-vacancy layer formation in diamond for wide-field quantum microscopy, Phys. Rev. Mater. 4 (10) (2020) 104605.

[23] K. Saarinen, P. Hautojärvi, C. Corbel, Positron annihilation spectroscopy of defects in semiconductors, in: Semiconductors and Semimetals, vol. 51, Elsevier, 1998, pp. 209–285.

[24] A. Haque, S. Sumaiya, An overview on the formation and processing of nitrogen-vacancy photonic centers in diamond by ion implantation, J. Manuf. Mater. Process. 1 (1) (2017) 6.

[25] G.R. Brandes, A.P. Mills, et al., Work function and affinity changes associated with the structure of hydrogen-terminated diamond (100) surfaces, Phys. Rev. B 58 (8) (1998) 4952.

[26] A.T. Collins, A. Connor, C.-H. Ly, A. Shareef, P.M. Spear, High-temperature annealing of optical centers in type-I diamond, J. Appl. Phys. 97 (8) (2005).

[27] M.I. Rakhmanova, A.Y. Komarovskikh, Y.N. Palyanov, A.A. Kalinin, O.P. Yuryeva, V.A. Nadolinny, Diamonds from the Mir Pipe (Yakutia): spectroscopic features and annealing studies, Crystals 11 (4) (2021) 366.

[28] S. Chakravarthi, C. Moore, A. Opsvig, C. Pederson, E. Hunt, A. Ivanov, I. Christen, S. Dunham, K.-M.C. Fu, Window into NV center kinetics via repeated annealing and spatial tracking of thousands of individual NV centers, Phys. Rev. Mater. 4 (2) (2020) 023402.